SANDIA REPORT

SAND200X-XXXX
Unlimited Release
Printed September 2016

Optimization of Isentropic Compression Loads on Current-Adder Pulsed Power Accelerator Architectures

D.B. Reisman, E.M. Waisman, B.S. Stoltzfus, W.A. Stygar, M.E. Cuneo, T.A. Haill , J.-P. Davis, J.L. Brown , C.T. Seagle, and R.B. Spielman

Prepared by
Sandia National Laboratories
Albuquerque, New Mexico 87185 and Livermore, California 94550

Sandia National Laboratories is a multi-mission laboratory managed and operated by Sandia Corporation, a wholly owned subsidiary of Lockheed Martin Corporation, for the U.S. Department of Energy's National Nuclear Security Administration under contract DE-AC04-94AL85000.

Issued by Sandia National Laboratories, operated for the United States Department of Energy by Sandia Corporation.

Available to DOE and DOE contractors from
U.S. Department of Energy
Office of Scientific and Technical Information
P.O. Box 62
Oak Ridge, TN 37831

Telephone: (865) 576-8401
Facsimile: (865) 576-5728
E-Mail: reports@osti.gov
Online ordering: http://www.osti.gov/scitech

Available to the public from
U.S. Department of Commerce
National Technical Information Service
5301 Shawnee Rd
Alexandria, VA 22312

Telephone: (800) 553-6847
Facsimile: (703) 605-6900
E-Mail: orders@ntis.gov
Online order: http://www.ntis.gov/search

SAND200X-XXXX
Unlimited Release
Printed September 2016

Optimization of Isentropic Compression Loads on Current-Adder Pulsed Power Accelerator Architectures

D.B. Reisman[1], E.M. Waisman[1], B.S. Stoltzfus[1], W.A. Stygar[1], M.E. Cuneo[1], T.A. Haill[1] , J.-P. Davis[1], J.L. Brown[1] , C.T. Seagle[1], R.B. Spielman[2]

[1]Sandia National Laboratories, Albuquerque, New Mexico 87185, USA
[2]Idaho State University, Pocatello, Idaho 83201, USA

Abstract

The Thor pulsed power generator is being developed at Sandia National Laboratories. The design consists of up to 288 decoupled and transit time isolated capacitor-switch units, called “bricks”, that can be individually triggered to achieve a high degree of pulse tailoring for magnetically-driven isentropic compression experiments (ICE). The connecting transmission lines are impedance matched to the bricks, allowing the capacitor energy to be efficiently delivered to an ICE strip-line load with peak pressures of over 100 GPa. Thor will drive experiments to explore equation of state, material strength, and phase transition properties of a wide variety of materials. We present an optimization process for producing tailored current pulses, a requirement for many material studies, on the Thor generator. This technique, which is unique to the novel “current-adder” architecture used by Thor, entirely avoids the iterative use of complex circuit models to converge to the desired electrical pulse. We describe the optimization procedure for the Thor design and show results for various materials of interest. Also, we discuss the extension of these concepts to the megajoule-class Neptune machine design. Given this design, we are able to design shockless ramp-driven experiments in the 1 TPa range of material pressure.

ACKNOWLEDGMENTS

The authors gratefully acknowledge J. Benage, M. Campbell, K. Kielholtz, K. LeChien, T. Mattsson, K. Matzen, D. Flicker, and R. Schneider.

CONTENTS

FIGURES

TABLES

1. INTRODUCTION

The magnetically-driven isentropic compression (ICE) technique was developed on the Z accelerator at Sandia National Laboratories [1,2]. The technique has been used over the past fifteen years for a variety of material studies. Currently the refurbished Z accelerator (also referred to as ZR) produces tailored current pulses to drive samples quasi-isentropically to pressures as high as 500 GPa [3]. Given the success of ZR, there has been a great interest in developing smaller, high-throughput generators for dynamic material experiments. This motivated the development of Thor, a compact generator based on a current-adder architecture. It has also motivated the development of the much larger megajoule-class generator Neptune.

In this article we present an optimization procedure aiding the design of Thor; a next-generation pulsed power generator that will achieve pressures as high as 100 GPa. The description of Thor and an introduction to the optimization procedure is given in a recent publication by the authors [4]. The purpose of this report is to provide a more in depth description of the optimization process as well as its generalization to all current-adder architectures.

The design of the Thor generator is briefly outlined in Sec. 2. A new algebraic technique that calculates the switch triggering sequence necessary to achieve a desired load current time history is described in Sec. 3. Application of the optimization technique to three examples of isentropic compression experiments on Thor is presented in Sec. 4. Optimization on the megajoule-class generator Neptune is discussed in Section 5. Section 6. contains our conclusions.

2. THOR CURRENT-ADDER PULSED POWER GENERATOR

Thor consists of the following components:

1. Up to 288 “bricks” which can be individually triggered. A brick is made of two capacitors connected in series to an electrically-triggered switch [5].
2. 288 coaxial cables which are impedance matched to the bricks. The cable transit-time length is chosen to be 300 ns in order to avoid wave reflections.
3. A central power flow (CPF) consisting of a tri-plate deionized (DI) water line that transitions to a single plastic-insulated line. The plastic-insulated line terminates in a strip-line load where current is concentrated.

Because Thor is modular in nature, we denote the configuration of the machine as “Thor-N”, where N is the number of bricks. As an example, the Thor-144 facility is shown in Fig. 1.

Each brick is approximately impedance matched to output cables which act as constant impedance transmission lines to the CPF. This is conceptually shown in Fig. 2. We consider bricks as each providing identical current shapes in time, $i(t)$, shown in Fig. 3. The peak current for a +/-110 kV capacitor charge is 42 kA with a rise time of ~60 ns. The optimal transmission line for an individual brick is given by

$$Z_1 = 1.1\sqrt{\frac{L_1}{C_1}} + 0.8R_1 \quad (1)$$

where L_1, R_1, and C_1 are the single brick inductance, resistance, and capacitance, respectively [6]. We define the optimum impedance to be that which maximizes the peak forward-going power at the input to the CFS. Using Eq. (1) and our single brick circuit parameters ($L_1 = 240nH, R_1 = 0.37\Omega, C_1 = 80nF$), we find that $Z_1 = 3\Omega$.

Strictly speaking, Thor is a current-adder architecture where brick currents are combined in parallel into the CPF. However, voltage can also be added at the brick level by using a Marx bank configuration. Here the bricks are added together as shown in Fig. 4. We see that for each additional stage two capacitors and a switch are added in series. Therefore, in an *m*-stage Marx bank arrangement, the brick current $i(t)$ remains the same compared to the regular brick case, while the brick output voltage is scaled by *m*. The brick circuit parameters become

$$L_m = mL_1, R_m = mR_1, C_m = C_1 / m \quad (2)$$

and the optimal transmission line impedance can be expressed as

$$Z_m = mZ_1 \quad (3)$$

Later we will use a combination of regular and “Marxed” brick to obtain an optimal current fit.

Typical strip-line load panels are 1.0 cm to 2.0 cm in width with a length approximately equal to twice the width. Load panels are made of either copper or aluminum and are separated by a Kapton-layered film package with a total thickness of 0.5 mm. The strip-line is designed to produce planar magnetic pressure loading. This configuration is used to produce a compressive wave that propagates through the electrode and sample material contained within the panel body.

3. OPTIMIZATION TECHNIQUE

3.1. Motivation

The ability to tailor the pressure pulse is desired to delay the onset of shocks in samples. Pulse shaping delays the intersection of loading characteristics. Ideally, the pulse shape can be tailored so that all characteristics intersect at a single "critical" location *Xc* [7,8]. Given the equation of state (EOS) of a material, ideal pressure waveforms can be calculated. In Fig. 5 we illustrate the construction of the ideal pressure waveform $P_I(t)$ for Aluminum compressed to 100 GPa. This waveform is constructed from the EOS for aluminum using Lagrangian wave characteristics which intersect at X_C=3.9 mm. The corresponding pressure histories from a 1D hydrodynamic simulation show simultaneous shock formation at $X \approx X_C$.

On the ZR machine pulse tailoring is performed by individually triggering gas switches into 36 transmission lines. A transmission line code is used, along with 2D MHD simulations that capture the dynamic load inductance, to determine the optimal switching sequence. Complicating the pulse shaping is the fact that the gas and water switches in each ZR module are not transit time isolated from the switches in the other modules. As a result, reflections from modules triggered early can interact with the switches in the modules triggered later in the pulse. This "cross-talk" complicates the ability to design and predict the desired current pulse. Currently, the circuit model for ZR contains over 50,000 elements. Design of a desired pulse typically takes a physicist several days of iterative simulation work. Furthermore, due to uncertainties in other factors such as current losses, dedicated pulse shaping experiments on ZR are often required to determine the optimal machine configuration for a particular experiment.

For a current-adder configuration such as Thor, we can take advantage of the transit time isolation of our bricks and determine our pulse without the use of a circuit or transmission line code. We note that this is unique to the current-adder architecture. Essentially this involves using the brick current waveforms as basis functions to construct the desired configuration. The forward going wave, and thus the forward going electrical power, in any of the constant impedance coaxial lines is independent of the load for the "clear time" of the system. We define the clear time τ_{clear} as the constant impedance line electromagnetic round trip time, counting from the first triggered brick. Furthermore, given that the load is at a small radius, only the voltage average and the total current of all bricks need to be considered [9].

3.2. Average voltage and total current

To clearly state our optimization procedure it is useful to differentiate currents and voltages in different sections of Thor. By V, I , we denote the average voltage and the total current at the CPF connecting circumference. V_k, I_k , indicate the voltage and current at the kth angular location on that circumference. The brick voltage and current are denoted by u_k, i_k . Using TEM waveguide theory, we may express the average voltage and total current as forward (+) and backward propagating (-) waves,

$$V = V_+ + V_- \quad (4)$$

$$I = \frac{V_+}{Z} - \frac{V_-}{Z} \quad (5),$$

where $V = \sum_{k=1}^{N} V_k / N,$ and $I = \sum_{k=1}^{N} I_k$, and N is the number of bricks.

We distinguish two relevant cases of N bricks with identical current shapes:

a) All the coaxial cables have the same impedance Z_1. In this case the impedance appearing in Eq. (5) is $Z = Z_1 / N$.

b) The coaxial lines are not all of the same impedance. In this case $Z = 1/\sum_{j=1}^{N} (1/Z_j)$, which reduces to case a) when $Z_j = Z_1, \forall j.$

We show in reference [18] that for both cases we obtain for the forward propagating quantities.

$$V_+ = \frac{1}{2}\left(V + ZI\right) \quad (6)$$

$$I_+ = \frac{1}{2}\left(\frac{V}{Z} + I\right) \quad (7)$$

In case a) Equations (6) and (7) are exact results, while for case b) they are approximate, as we discuss in the Appendix. We remark that the average voltage and total current are the relevant quantities because the load is at small radius, where angular variations are negligible for the long wavelength electrical pulses employed by Thor [9].

Since the bricks are transit-time decoupled and the transmission lines are of constant impedance, the forward-going current is the sum of all individual forward-going currents at the CPF.

$$I_+ = \sum_{k=1}^{N} i_{k+}\left(t - \tau_k\right) \quad (8)$$

where $\bar{\tau} = \left(\tau_1, ..., \tau_n\right)$ is the set of brick delay times. During τ_{clear} the brick current

$$i_{k+}(t) = i(t - l/c_{coax}) = u_k(t - l/c_{coax})/Z_k \ . \quad (9)$$

That is, the kth forward propagating brick current and voltage equals the kth time translated brick current. Neglecting attenuation, the forward-going current (or voltage) is equal to the brick

current, until reflections from the brick can reach back to the CPF. The clear time for all the equal length coaxial lines is $2l / c_{coax}$. If we take as zero time the arrival of the earliest triggered time pulse to the CPF, no reflections affect any of the brick forward-going pulses at that location for the period going from zero time to the system clear time, i.e., $0 \le t \le \tau_{clear} = 2l / c_{coax}$. Moreover, during that period, the forward-going current of a given brick at the CPF connection location, is the time translated current for that brick, which is the meaning of Eq. (9). Using the desired ICE load voltage and current (V_D, I_D) and the inductance of the CPF between the load and the cable header (L_C), we may determine our desired forward-going current:

$$I_{0+} = \frac{1}{2}\left[\frac{V_D + L_C \dot{I}_D}{Z} + I_D\right] \quad (10)$$

We remark that for convenience we have lumped the DI water transmission line element of the CPF into the impedance L_C. This is a reasonable approximation since the water line transit time of ~20 ns is much shorter than the typical current rise time of 200-500 ns.

We then perform an optimization procedure to determine a set of τ_k such that $I_{0+} \approx I_+$. This involves finding an "adequate" local minimum to the L_2 norm given by

$$F(\vec{\tau}) = \int_0^T dt\left[I_+(t) - I_{0+}(t)\right]^2 \quad (11)$$

3.3. Summary of procedure

1. Determine desired current and voltage at load: I_D, V_D. Typically this is done using a MHD code where these quantities can be determined self-consistently.
2. Form the forward-going component of the total current I_{0+} at the connecting point given by Eq. (10).
3. Require the sum of the forward components of the brick currents be as close as possible to I_{0+}; that is:

   $$I_+ = \sum_{k=1}^{N} i_{+k}(t - \tau_k) = \sum_{k=1}^{N} i(t - \tau_k) \approx I_{0+} \quad (12)$$

   where $\vec{\tau}$ is the delay time set given by

   $$\vec{\tau} = (\tau_1, ..., \tau_n)$$

   and Eq. (12) is valid for $0 \le t \le \tau_{clear}$.
4. Minimize the difference between I_+ and I_{0+} by finding the local minimum of the L_2 norm $F(\vec{\tau})$ given by Eq. (11), employing a gradient-based technique to find the optimal delay times $\vec{\tau}$.

3.4. Consideration of attenuation

The only important effect of attenuation, if it is not too large, is the uniform decrease of amplitude in the brick forward currents and corresponding voltages, as they arrive at the CPF connecting point. To confirm this assertion we take the coaxial cable resistance for the length of the cable corresponding to attenuation measurements. Based on measurements of the existing Thor cable at the characteristic frequency of 2 MHz, we take the resistance of each 300 ns transit time brick cable package to be R_C=0.56 Ω. Using these values for impedance and resistance we solve the telegrapher's equations numerically. In Fig. 6 we show the brick current after it has propagated to the end of one of the coaxial lines into a matched impedance. We see that the reflections are negligible, and that the signal shape is the same as the brick current multiplied by a factor of 0.9.

5. EXAMPLES

For examples we consider three materials that demonstrate the various aspects of the current-adder architecture as combined with the optimization technique. The first example is cerium, a relatively "soft" metal (low bulk modulus), with a complex phase diagram. We will consider the compression of cerium up to 40 GPa where the material is compressed through the γ, α, and ε phases [10]. This requires an aluminum electrode drive pressure of 33 GPa. When the γ-α phase boundary line is crossed, cerium undergoes a volume collapse resulting in a two-wave structure in the compressive wave. It should be noted that the pressure drive for cerium is considered closest-to-ideal as the low pressure phase transition prevents an ideal intersection of loading characteristics.

The second example is tantalum. Here we wish to compresses the material shocklessly, hold it a constant pressure for ~100 ns, and finally release the material into a LiF window. The purpose of this design is a well-defined release wave whereby the material strength can be extracted through Lagrangian analysis [11]. The target copper electrode drive pressure for this design is 89 GPa, which gives a tantalum sample drive pressure of 110 GPa.

The third example is aluminum, a standard electrode material for driving "soft" metals such as the aforementioned cerium. Aluminum is also a standard material for magnetically-driven flyer plates. In the case of flyer plates, impact measurements are performed to characterize Hugoniot states. Similar to ICE, a shockless flyer plate is desired so as to have well-characterized state for solving the jump conditions [12]. We consider shockless compression to ~100 GPa which requires a higher applied load voltage than, for example, copper as well as a more exponential-like wave shape in both current and voltage.

For each material example, we use the ALEGRA MHD code [13] to iteratively determine the current $I_D(t)$ and voltage $V_D(t)$ such that the magnetic pressure $P_{MAG}(t)$ approximates the ideal drive pressure $P_I(t)$:

$$P_I(t) \approx P_{MAG}(t) = B^2(t)/2\mu_0 \quad (13)$$

where $B(t)$ is the magnetic field magnitude in the center of the insulating gap between the two drive panels. The pressure waveforms for all three examples are shown in Fig. 7. It should be noted that magnetic diffusion, which produces joule heating and ablation at the electrode surface, alters the ideal pressure drive applied to the sample. In practice the magnetic drive history must be slightly modified to maintain approximately ideal loading conditions. This process, which involves the use of a MHD code along with backward integration, is described in the literature [7]. The desired current and voltage waveforms are shown in Fig. 8. The details of each design are summarized in Table 1 where we also include the baseline 100 GPa copper design from reference 4.

Using Eq. (10) we calculate the desired forward-going current that appears on the CPF after the TEM wave has propagated through the coaxial transmission lines. In this case, the

central power-flow inductance is given by L_C=1.8 nH and the transmission line impedance is given by

$$Z = Z_1 / N \quad (14)$$

where Z_1 is the single-brick effective cable impedance and N is the total number of bricks.

We form $F(\bar{\tau})$ given in Eq. (11), using the appropriate brick basis functions $i(t)$ (Fig 3), and find a "good" local minimum. The optimization code is written in the Python programming language and uses optimization routines from the SciPy software package [14]. Specifically, a truncated Newton-conjugate gradient (TNC) method is used to find an adequate local minimum of the L_2 norm given in Eq. (11). The TNC method iteratively solves the Newton equations under the constraint of each variable having an upper and lower bound [15]. In our case those bounds are $\tau_{\min}$ and $\tau_{\max}$ - the minimum and maximum trigger times.

As in most optimization algorithms an initial guess must be provided. It is sufficient for these examples to choose a set of equally spaced trigger times from $\tau_{\min}$ to $\tau_{\max}$. For all the example cases we organize our bricks into groups of eight bricks, where in each group the bricks share the same trigger time.

For the cerium and tantalum examples we consider Thor configurations consisting of 144 bricks and 200 bricks, respectively. The results of the optimization procedure are shown in Fig. 9. We see that a reasonable fit is obtained between the optimized forward-going current (I_+) and the desired forward-going current (I_{0+}).

For the tantalum case, we verify the closeness of fit of the resulting pressure waveforms using the MHD code. For this we form the circuit driven by the open circuit voltage. From Eq. (10) we obtain

$$V_{OC} - ZI_D - L_C \dot{I}_D = V_D \quad (15)$$

where $V_{OC} = 2ZI_{0+}$ is the open circuit voltage. This is simply an inductance-resistance (LR) circuit that can be applied to our MHD calculation. The results of the MHD calculation for both the desired and the optimized voltage-driven cases are shown in Fig. 10. We see good agreement between the desired and optimized pressures during the shockless ramp phase. We note some difficulty in obtaining the flatness of the pressure drive. However, in practice this is acceptable.

For the aluminum case we consider a Thor configurations consisting of up to 288 bricks. We use this example to illustrate the procedure using "mixed" bricks. Here we combine our regular bricks with bricks arranged in a two-stage Marx configuration. According to Eq. (3) the two-stage (m=2) Marxed brick will have a transmission line impedance of $Z_2 = 2Z_1$ and a voltage of $2u_k$.

The motivation behind using mixed bricks is that we require a relatively high final voltage (150 kV) at the load for the aluminum case. It is clear that the regular bricks cannot provide this peak voltage as the load voltage they provide is generally less than 100 kV. We denote the number of regular bricks by N_1 of impedance Z_1 and the number of Marxed bricks as N_2 of impedance $Z_2 = 2Z_1$. Thus, the total number of bricks is given by $N=N_1+N_2$. We consider combinations ranging from all regular bricks (N_1=288, N_2=0) to all Marxed bricks (N_1=0, N_2=216). This is conceptually shown in Fig. 11. The results for four combinations of regular and Marxed bricks are shown in Fig. 12. The best fit is obtained, as expected, with all Marxed bricks. An adequate fit is obtained with a half-and-half configuration (N_1=144, N_2=144). For all the cases we have used $Z_1 = 3\Omega, Z_2 = 6\Omega$.

To verify the assumptions in case b) are correct, we calculate the total current in the load given our set of optimized delay times. For this we use the Screamer circuit code, which includes individual brick LRC circuits connected to the CPF through transmission lines of the appropriate impedance [16,17]. The CPF is treated as a constant inductor connected in series to the MHD-calculated load inductance.

Since our results should be independent of brick-type ordering, we consider three cases with the half-and-half mixed brick case: (1) All Marxed bricks triggered last; (2) All Marxed bricks triggered first; and (3) A random ordering of Marxed and regular bricks. The results are shown in Fig. 13. We see that all three cases, calculated using Screamer, are closely matched with each other. Also, the results are in good agreement with the desired current pulse, thus further validating the approximation we introduced for the mixed brick case.

The results shown in Figure 13 are confirmation of our previous assertion: because the load is at small radius, only the average voltage needs to be considered. Thus, as long as the triggering is such that the desired average voltage is well approximated, the quality of the fit does not depend on the brick triggering order. Also, as a further consequence, the fit does not depend on geometrical factors such as the number or location of the cables on the CPF.

In practice, we have found a useful guide in determining the optimal number and type of bricks, given a desired ICE design. First, we note that the energy delivered to CPF, including the load, is typically one quarter of the total electrical energy when pulse tailoring is invoked. We observed this in the many optimization calculations we have performed. We therefore use this rule-of-thumb in the following discussion. For the case of the regular and Marxed bricks, this can be expressed as

$$\frac{4E_{CPF}}{Z_1\eta} = N_1 + 2N_2 \quad (16)$$

The CPF electrical energy is given by

$$E_{CPF} = \int_0^T I_D \left(V_D + L_C \dot{I}_D \right) dt, \quad (17)$$

where T is the pulse time, and the brick energy integral is

$$\eta = \int_0^{T_B} i^2(t) dt \, , \quad (18)$$

where T_B is the time after which the current is negligible.

Second, we note that for maximum energy efficiency the total cable impedance Z should be approximately equal to some averaged value of the CPF impedance measured at the connecting point. This can be expressed as

$$\frac{Z}{\bar{Z}_{CPF}} = N_1 + \frac{N_2}{2} \quad (19)$$

where the energy-weighted average inductance is given by

$$\bar{Z}_{CPF} = \frac{\int_0^T Z_{CPF} P_{CPF} \, dt}{\int_0^T P_{CPF} \, dt} = \frac{\int_0^T \left(V_D + L_C \dot{I}_D \right)^2 dt}{\int_0^T P_{CPF} \, dt} \quad (20)$$

and the time-dependent CPF power and impedance are given by

$$\begin{aligned} Z_{CPF} &= \left(V_D + L_C \dot{I}_D \right) / I_D, \\ P_{CPF} &= \left(V_D + L_C \dot{I}_D \right) I_D. \end{aligned} \quad (21)$$

Therefore, given our desired voltage and current, we may solve Eq. (16) and (17) to determine brick numbers N_1 and N_2. Using our aluminum case we find that the optimal configuration is given by N_1=8, N_2=207. This is very close to our best-case shown in Fig. 12 which was given by N_1=0, N_2=216. In fact, we see that the total cable impedance Z for this example is very close to its energy-weighted average $\bar{Z}_{CPF}$ (Fig. 14).

To demonstrate the effects of attenuation on the optimization process, we again consider the aluminum example $(N_1 = 144, N_2 = 144)$ with resistive transmission lines. Including the aforementioned cable resistance the circuit calculations gives us a current waveform that undershoots the desired waveform by approximately 10%. This assumes the previously determined trigger time set $\vec{\tau}$. To compensate for the cable attenuation, we utilize as basis functions attenuated brick currents, including the resistive effect, which as we described above consists of simply replacing $i(t)$ by $0.9i(t)$. The corrected current waveform becomes the "attenuated" brick basis function and is used in the optimization procedure to find a new set of

trigger times $\vec{\tau}'$. The results of using the new trigger time set $\vec{\tau}'$ in a circuit calculation are shown in Fig. 15. We see that this modified procedure is successful in producing a total current that is close to the desired current waveform.

6. NEPTUNE

6.1. Motivation and machine design

The ZR machine uses conventional, state-of-the-art, pulsed power technology to achieve high pressures. Recently, we have developed the "current adder" architecture to overcome some of the limitations of standard pulsed-power machines. One of these limitations is the difficulty in producing tailored pulses with internal voltage reflections from the closely coupled Marx banks. Another limitation is the energy delivery inefficiency caused by the need for multiple stages of pulse compression.

We have extended the current adder concept to design a machine capable of 1 TPa level performance. This machine, called Neptune, consists of N=600 independent impedance-matched bricks [19]. Each brick is an 8-stage Marx generator (the case of m=8 in Eq. 2 and 3) which produces a 52 kA current pulse with a rise time of 100 ns. Neptune stores 4.8 MJ of electrical energy in its brick capacitors. A τ=450 ns long water insulated coaxial transmission line transports the power generated by each brick to a system of 12 electrically parallel water-insulated conical transmission lines. The coaxial lines ensure that transit-time isolation is maintained for the clear time of τ=900 ns. Impedance matching is maintained between the bricks (Z_B) , the coaxial lines (Z_1), and the system of conical lines (Z_W). This can be expressed as

$$Z = \frac{Z_B}{N} = \frac{Z_1}{N} = Z_W \quad (22)$$

where Z is the effective impedance.

The conical water lines are connected electrically in parallel by a water-insulated convolute. The convolute sums the electrical currents at the conical lines, and delivers the combined current to a single solid dielectric insulated radial transmission line. The radial line in turn transmits the combined current to the physics load. The Neptune concept is shown in Fig. 16.

As in the case of Thor, current-adder machines like Neptune can be thought of consisting of three components: 1) Bricks that provide the current; 2) constant impedance transmission lines; and 3) a central power flow section (CPF) where the currents are combined and delivered to the physics load. Using the desired ICE load current and voltage (I_D, V_D) we may determine our desired forward-going current I_{0+}.

The desired current and voltage are found iteratively through two and three dimensional magnetohydrodynamic (MHD) modeling of the strip-line load. This accomplished by specifying a magnetic pressure drive (Eq. 13).

6.2. ZR-level performance designs

We consider using Neptune to reproduce two major experimental platforms that are currently being fielded on the ZR machine. The first is an aluminum flyer plate capable of reaching a velocity of 30 km/s. As mentioned earlier, these impact experiments are used to determine Hugoniot states in materials. The second experiment is a high-pressure metal, tantalum; ramp compressed up to 600 GPa. This design produces shockless loading of the tantalum, allowing a quasi-isentrope to be determined up to peak pressure. In both cases we use 2D MHD calculations to determine the desired electrical quantities I_D and V_D. We note that these specific calculations were originally used to design experiments on ZR, Design parameters and load performances are summarized in Table 2.

The aluminum flyer plate design consists of panels of length 20 mm and width 15 mm . The AK gap is 1 mm and the aluminum flyer plate thickness is 1 mm. 60 brick-groups are chosen to perform the optimization. The results of the optimization are shown in Fig 17 (a), where optimized trigger times are determined to produce a best match to the desired forward-going current. As discussed in section 5, we perform a 2D MHD calculation using the optimized open-circuit voltage (Eq. 15). This is simply a series circuit consisting of the resistance Z, the inductance L_C, and the computational strip-line element. The circuit is driven by the open-circuit voltage $V_{OC}=2ZI_+$. We see in Fig. 17 (b) that we obtain good agreement between our "optimized" total current, the result of our trigger time set $\vec{\tau}$, and our original "desired" total current.

The tantalum design consists of copper panels of length 20 mm and width 11.6 mm. The AK gap is 1 mm and the copper driver plate thickness is 1 mm. 40 brick-groups are chosen to perform the optimization. The results of the optimization are shown in Fig 18. Again we obtain excellent agreement between optimized and desired quantities, thus ensuring that shockless loading can be maintained to a peak pressure of 600 GPa in this design.

6.3. 1 Tpa designs

We consider copper shocklessly ramp-compressed to 1 TPa over a time scale of 600 ns. Under these conditions copper will be driven from its ambient density of 8.93 g/cm^3 to a density of approximately 19 g/cm^3. Copper is of great interested because it is used on the ZR machine as a driver material for many material physics experiments. Also, copper is being used as a standard on other high-pressure experimental platforms [20].

Typically, an "ideal" pressure drive is determined from the condition of intersecting loading characteristics at the Lagrangian "shock-up" distance X_C. For instance, for the 600 ns drive considered here, X_C=2.2 mm. In practice, the pressure drive must be modified to account for magnetic diffusion into the electrode, which alters the pressure drive. This modification is performed through iterative 1-D calculations with an optimization program. The final results of this process are shown in Fig. 19 where the B-field drive is determined to obtain a shockless free surface velocity profile in a 1.8 mm copper sample. This B-field is in turn used to determine the magnetic pressure given in Eq. 3.

The panel dimensions are carefully chosen to meet the current, energy, and voltage requirements for reaching 1 TPa in magnetic pressure. It should be noted that several geometric

and temporal factors affect the design of the strip-line load, given limitations in the electrical quantities. First, panel width can be adjusted to achieve the current density necessary to reach the target pressure. Second, panel length can be adjusted to limit the voltage and energy delivered to the load. Third, since ideal pressure waveforms are self-similar in time, the rise time can be scaled to limit the total energy delivered to the load. It should also be noted that slight modifications, not considered here, such as panel tapering can be employed to improve drive planarity. We find that an optimal configuration for panels of length 12 mm and width 6 mm with the aforementioned current rise time of 600 ns.

We performed 3D MHD calculations on a representative strip-line load to determine the I_D and V_D that will reproduce the magnetic pressure drive P_{MAG}. Peak I_D and V_D are 14 MA and 780 kV, respectively. 1 MJ of electrical energy is delivered to the load. Cross sections of the 3D strip-line are shown in Fig. 20 at the initial time T=0 ns and the peak compression time of T=600 ns. During compression, the anode-cathode gap is expanded from the initial 1 mm width to a final gap width of ~3 mm. Correspondingly the inductance grows from an initial value of 2.5 nH to a final value of 6.3 nH.

Our electrical quantities I_D and V_D are used to construct the forward-going voltage given in Eq. 2. Transmission line impedance and CPF inductance are given by Z=0.0275 Ω and L_C=3.0 nH, respectively. To perform the optimization, we consider all 600 brick with 100 trigger points. Performing the optimization outlined in Eq. 2 we obtain our optimized triggering sequence and best-fit to the desired forward-going current [Fig. 21 (a)].

As a check on our procedure we apply the open-circuit voltage obtained from our optimization process to a Neptune circuit model self-consistently coupled to the 3D MHD calculation. As before, the circuit is driven by the open-circuit voltage $V_{OC}=2ZI_{+}$.The results of the calculation are shown in Fig. 21 (b). We see that pressure drive obtained from the optimization procedure is in good agreement with our desired pressure drive.

In summary, we have shown that a new pulsed power driver, called Neptune, is capable of performing magnetically-driven shockless ramp experiments in the range of 1 TPa of pressure. The design, which uses a current-adder architecture, enables the rapid determination of shaped current pulses that are required for shockless loading. This is accomplished by an algebraic optimization technique that takes advantage of the time-transit isolated current pulses produced by the 600 brick circuits in the design. The copper ICE design presented here represents one of many ~1 TPa designs that could be fielded on Neptune. For instance, using copper as the driver electrode, experiments with tantalum, lead, and iron could be performed in the same pressure range.

7. CONCLUSIONS

The Thor current-adder design uses multiple capacitor-driven brick switches to deliver current to a power flow structure via impedance matched, transit-time-isolated coaxial cables. The current is concentrated into a strip-line load where dynamic material experiments can be performed using the large magnetic pressures. Because of the decoupling of the individual bricks, current can be tailored to achieve shockless loading. This is done through an optimization procedure that uses the individual brick current waveforms as basis functions in building the

desired total current pulse. This effective and fast technique can be used to design precisely tailored waveforms for a variety of material experiments. It may also be generalized to all current-adder architectures that maintain transit-time decoupling of the bricks, including machines that contain different combinations of voltage-added or “Marxed” bricks. Ultimately, this optimization technique can be applied to efficiently design 1 TPa-level material experiments on next-generation current-adder pulsed power machines such as Neptune.

8. REFERENCES

1. D. B. Reisman, A. Toor, R. C. Cauble, C. A. Hall, J. R. Asay, M. D. Knudson, and M. D. Furnish, J. Appl. Phys. **89**, 1625 (2001).
2. C. A. Hall, J. R. Asay, M. D. Knudson, W. A. Stygar, R. B. Spielman, T.D. Pointon, D. B. Reisman, A. Toor, and R. C. Cauble, Rev. Sci. Instrum. **72**, 3587 (2001).
3. J.-P. Davis, J. L. Brown, M. D. Knudson, and R. W. Lemke, J. Appl. Phys. **116**, 204903 (2014).
4. D.B. Reisman, B.S. Stoltzfus, W.A. Stygar, K.N. Austin, E.M. Waisman, R.J. Hickman, J.-P. Davis, T.A. Haill, M.D. Knudson, C.T. Seagle, J.L. Brown, D.A. Goerz, R.B. Spielman, J.A. Goldlust, and W.R. Cravey, Phys. Rev. ST Accel. Beams **18**, 090401 (2015).
5. J. R. Woodworth, J. A. Alexander, F. R. Gruner, W. A. Stygar, M. J. Harden, J. R. Blickem, G. J. Dension, F. E. White, L. M. Lucero, H. D. Anderson, L. F. Bennett, S. F. Glover, D. Van DeValde, and M. G. Mazarakis, Phys. Rev. ST Accel. Beams **12**, 060401 (2007).
6. W. A. Stygar, M. E. Cuneo, D. I. Headley, H. C. Ives, R. J. Leeper, M.G. Mazaratis, C. L. Olson, J. L. Porter, T. C. Wagoner, and J. R. Woodworth, Phys. Rev. ST Accel. Beams **10**, 030401 (2007).
7. J.-P. Davis, C. Deeney, M. D. Knudson, R. W. Lemke, T. D. Pointon, and D. E. Bliss, Physics of Plasmas **12**, 056310 (2005).
8. T. Ao, J.R. Asay, S. Chantrenne, M.R. Baer, and C.A. Hall, Rev. Sci. Instrum. **79**, 013903 (2008).
9. E.M. Waisman and A. Wilson, J. Appl. Phys. 53, 731 (1982).
10. V. M. Elkin, V. N. Mikhaylov, A. V. Petrovtsev, and F. J. Cherne, Phys. Rev. B **84**, 094120 (2011).
11. J. L. Brown, C.S. Alexander, J.R. Asay, T.J. Volger, and J.L. Ding, J. of Appl. Phys. **114**, 223518 (2013).
12. R. W. Lemke, M.D. Knudson, and J.-P. Davis, *Int. J. Impact. Eng.* **38,** 480 (2011).
13. A. C. Robinson, T. A. Brunner, S. Carroll, R. Drake, C. J. Garasi, T. Gardiner, T. Haill, H. Hanshaw, D. Hensinger, D. Labreche, R. W. Lemke, E. Love, C. Luchini, S. Mosso, J. Niederhaus, C. C. Ober, S. V. Petney, W. J. Rider, G. Scovazzi, O. E. Strack, R. M. Summers, T. G. Trucano, V.G. Weirs, M. W. Wong, and T. Voth, in Proceedings of the 46th AIAA Aerospace Sciences Meeting and Exhibit, Reno, NV, January 7–10, 2008, Paper No. AIAA-2008-1235.
14. SciPy: Open Source Scientific Tools for Python, http://www.scipy.org.
15. S. G. Nash, *SIAM J. Numer. Anal.*, **21** (4), 770 (1984).
16. M. L. Kiefer and M. M. Widner, in *Proceedings of the 5th IEEE International Pulsed Power Conference*, edited by M. F. Rose and P. J. Turchi (IEEE, Piscataway, NJ, 1985), p. 685.
17. M. L. Kiefer, K. L. Shaw, K.W. Struve, M. M. Widner, and R. B. Spielman, SCREAMER, a pulsed power design tool, user's guide for version 3.2.4.2 (2008).
18. E.M. Waisman, D.B. Reisman, B.S. Stoltzfus, W.A. Stygar, M.E. Cuneo, J.-P. Davis, T.A. Haill, J.-P. Davis, J.L. Brown, C.T. Seagle, R.B. Spielman, Rev. Sci. Instrum **87**, 063906 (2016).

19. W. A. Stygar, D. B. Reisman, B. S. Stoltzfus, K. N. Austin, J. F. Benage, E. W. Breden, R. A. Cooper, M. E. Cuneo, J.-P. Davis, J. B. Ennis, P. D. Gard, G. W. Greiser, F. R. Gruner, T. A. Haill, B. T. Hutsel, P. A. Jones, K. R. LeChien, J. J. Leckbee, S. A. Lewis, D. J. Lucero, G. R. McKee, J. K. Moore, T. D. Mulville, D. J. Muron, S. Root, M. E. Savage, M. E. Sceiford, R. B. Spielman, E. M. Waisman, and M. L. Wisher, Phys. Rev. Accel. Beams **19**, 070401 (2016).
20. R. G. Kraus, J.-P. Davis, C. T. Seagle, D. E. Fratanduono, D. C. Swift, J. L. Brown, and J. H. Eggert, Phys. Rev. **B** 93, 134105 (2016).

9. FIGURES

.

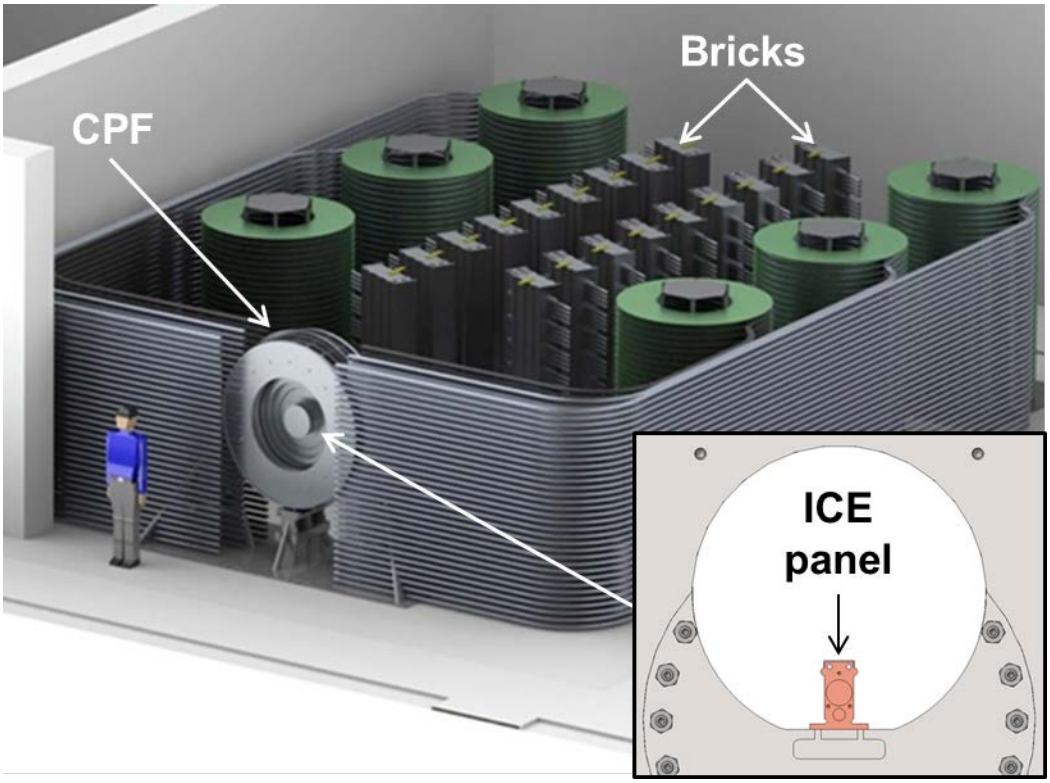

Figure 1. Thor-144 facility consisting of 144 bricks. Shown are the brick towers, cable runs, and the CPF. Inset shows ICE panel in center section where current is concentrated. Ultimately Thor will be extended to Thor-288, the maximum capability of 288 bricks.

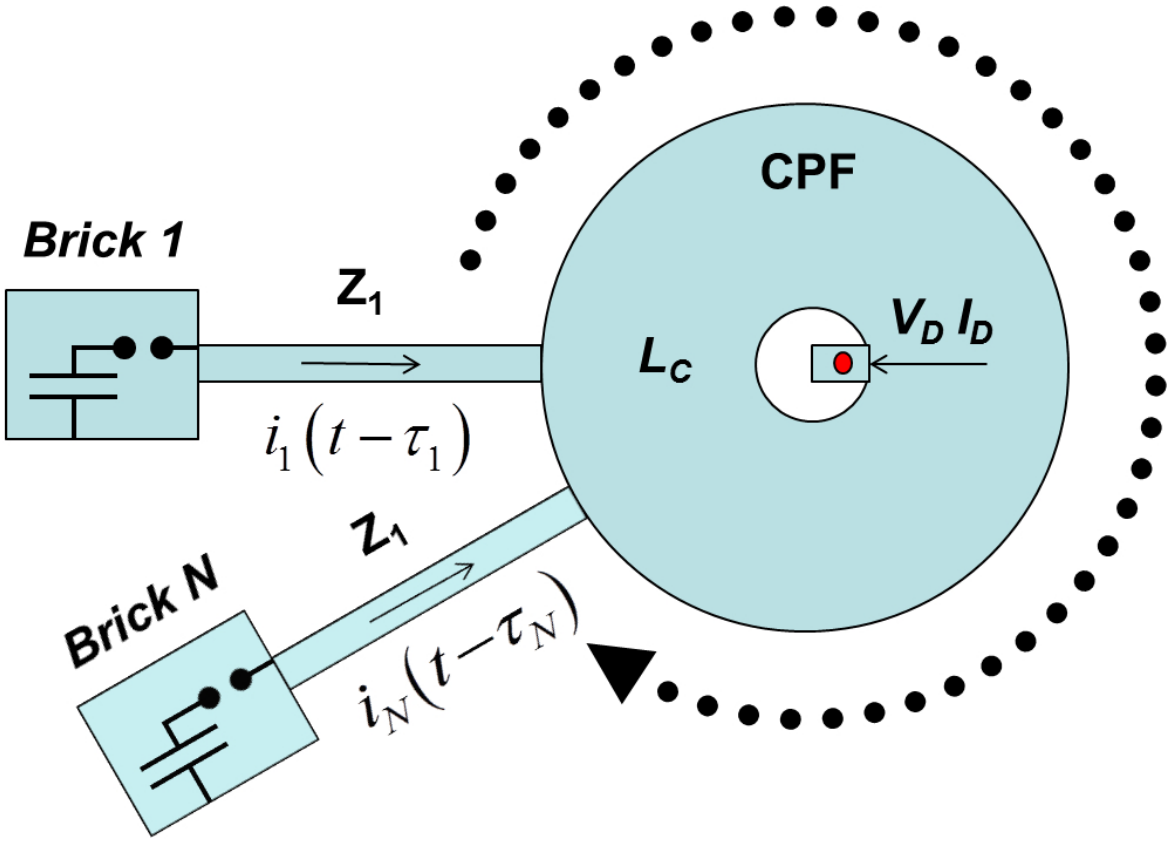

Figure 2**.** Conceptual drawing of the Thor current-adder architecture. Current from N bricks is added in parallel using transmission lines which connect to the CPF. There the current is concentrated into the strip-line load. The equations corresponding to this " circuit-like" diagram are in Section 3.2 (case a).

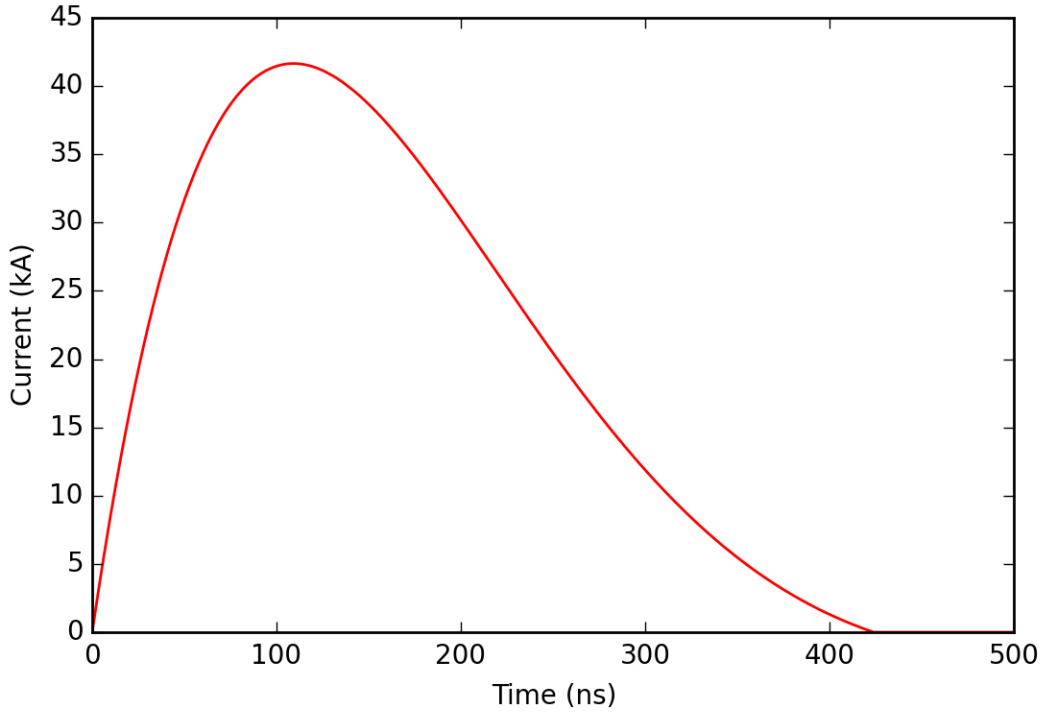

Figure 3. Brick current $i(t)$.

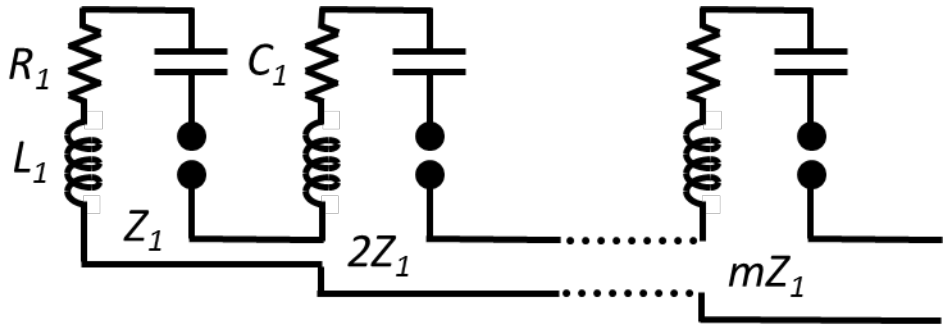

Figure 4. Circuit diagram showing the arrangement of *m* bricks into an *m*-stage Marxed brick.

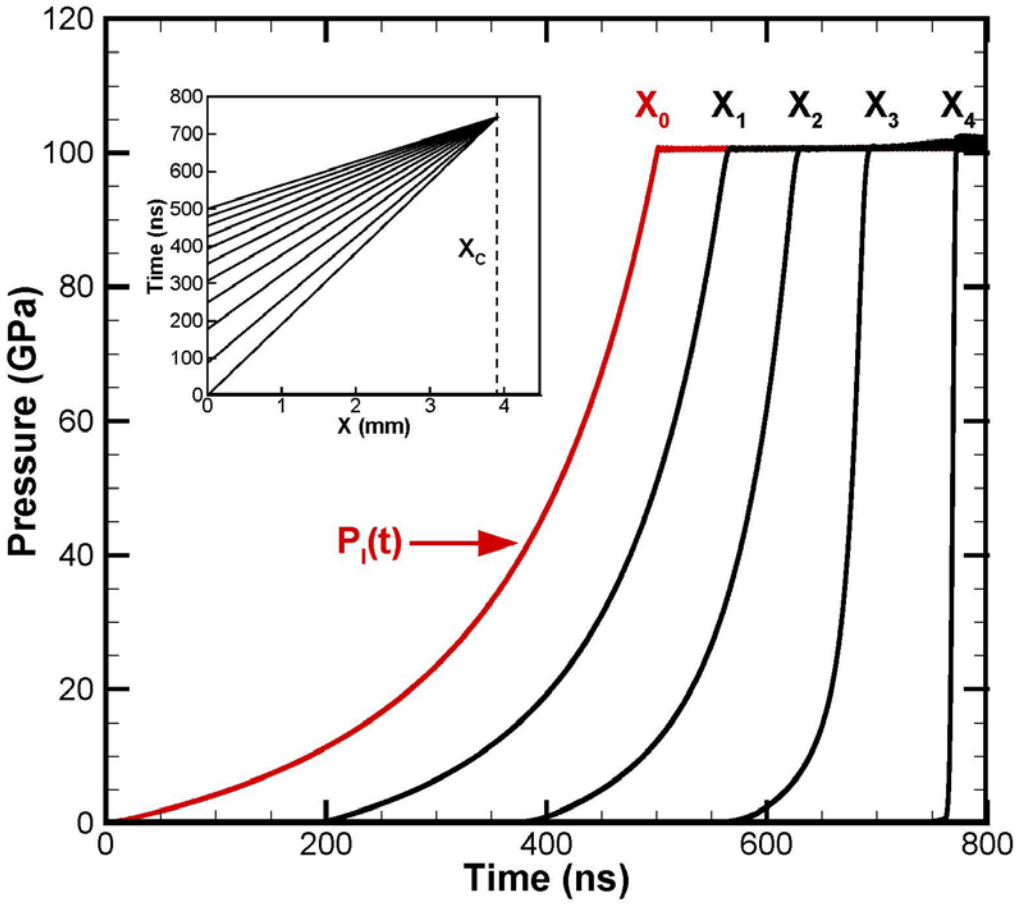

Figure 5. Aluminum compressed to 100 GPa with a tailored pressure pulse $P_I(t)$. Pressure profiles are shown at Lagrangian distances in the sample from X=0 mm to X=4 mm, in steps of 1 mm. A shock is formed simultaneously along the full pressure range at X=4 mm. Inset shows construction of ideal waveform in Lagrangian t-X coordinate space where characteristics intersect at X_C=3.9 mm.

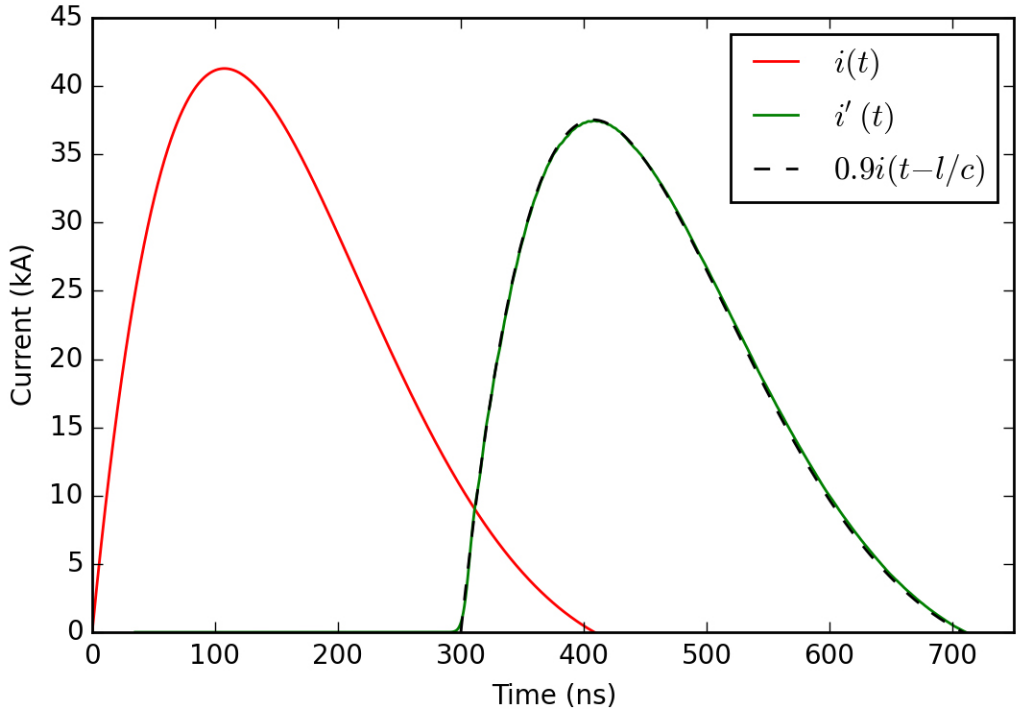

Figure 6. Attenuated cable signal $i'(t)$ after transmission through a 300 ns line and into an impedance matched load. This is equivalent to a scaled brick current of $0.9i\left(t-l/c\right)$.

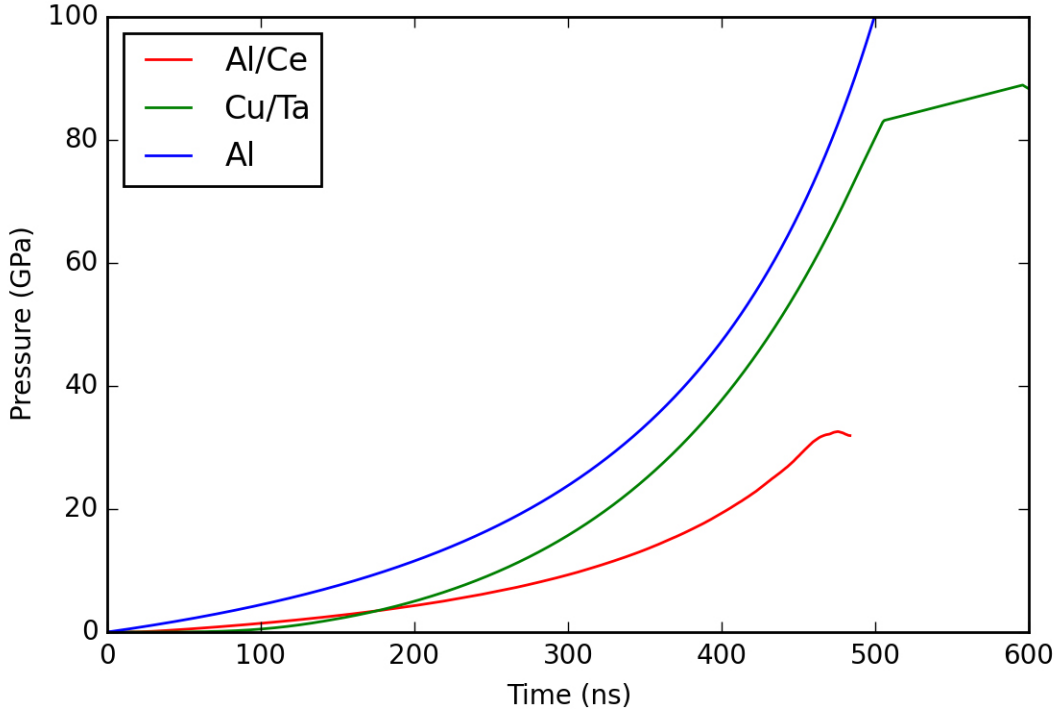

Figure 7**.** Pressure waveforms P_{MAG} for the three example cases.

(a)

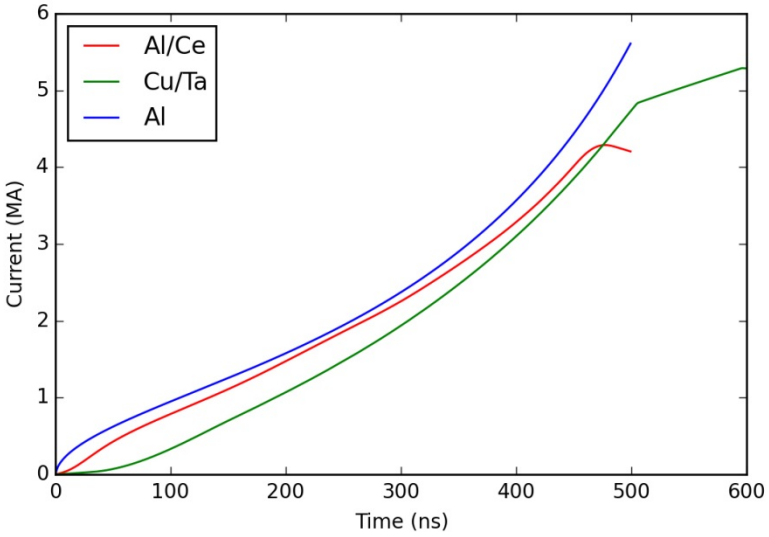

(b)

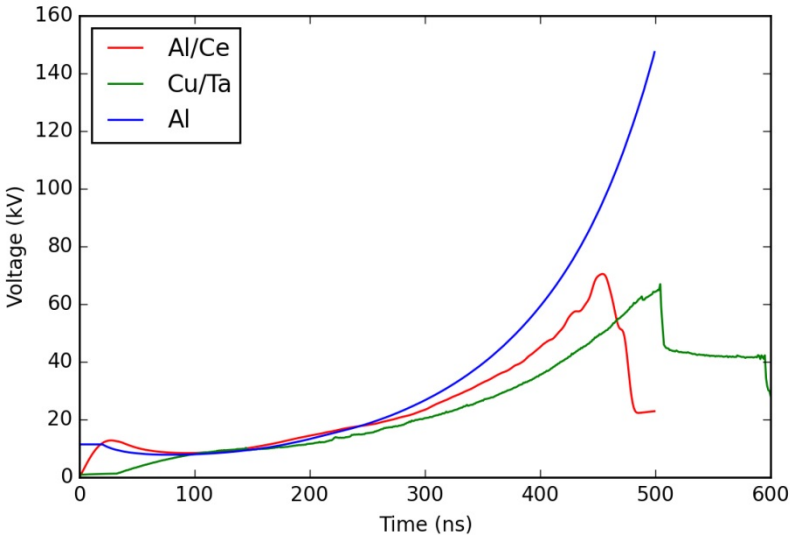

Figure 8. (a) Desired current waveforms I_D and (b) voltage waveforms V_D for the three example problems.

(a)

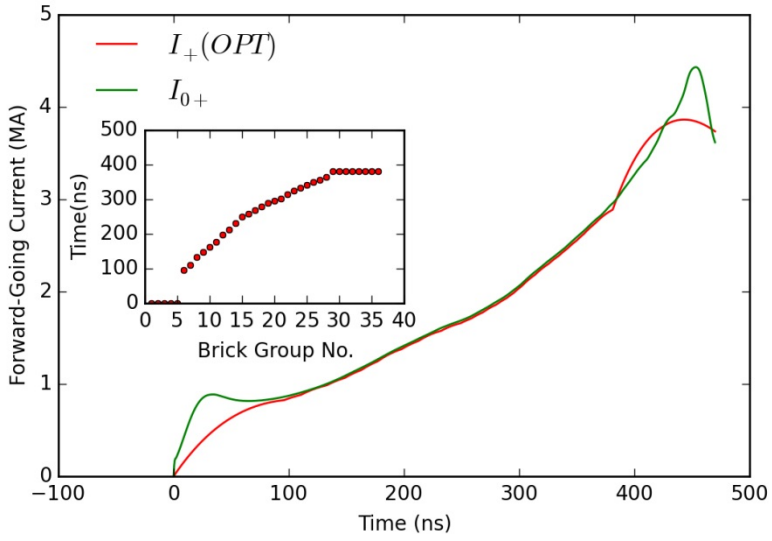

(b)

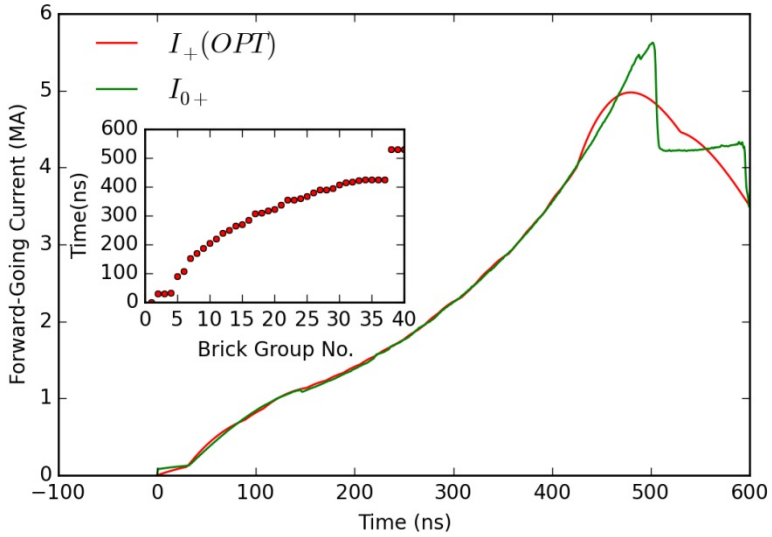

Figure 9. (a) Cerium optimizations results for 144 bricks and 36 trigger times. (b) Tantalum optimization results for 200 bricks and 40 trigger times. Shown for each case are the optimized fit of the forward-going current to the desired forward-going current. Insets show the optimized trigger times $\vec{\tau}$ for each example.

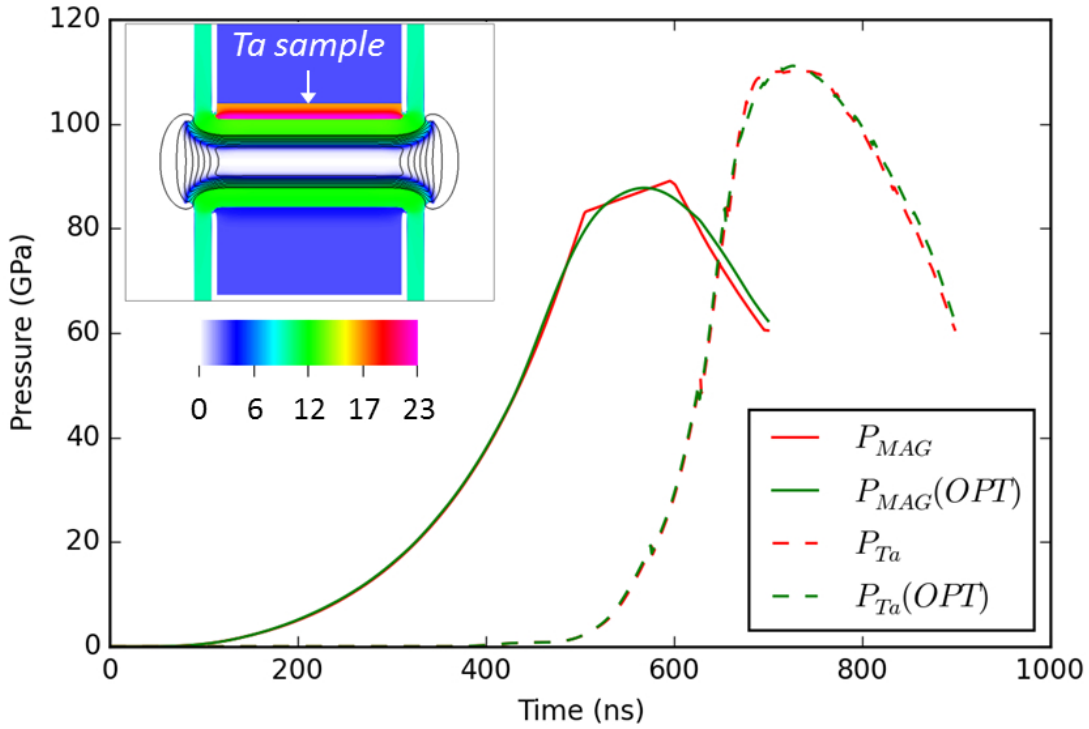

Figure 10. Desired pressure waveforms compared with MHD-calculated pressures using the optimized open circuit voltage (OPT). Shown are both the magnetic pressure driving the copper electrode (P_{MAG}) as well as the pressure driving the tantalum sample (P_{Ta}). Inset shows the 2D MHD calculation at 700 ns. Inset color contours are density (g/cm^3) and lines are contours of P_{MAG} .

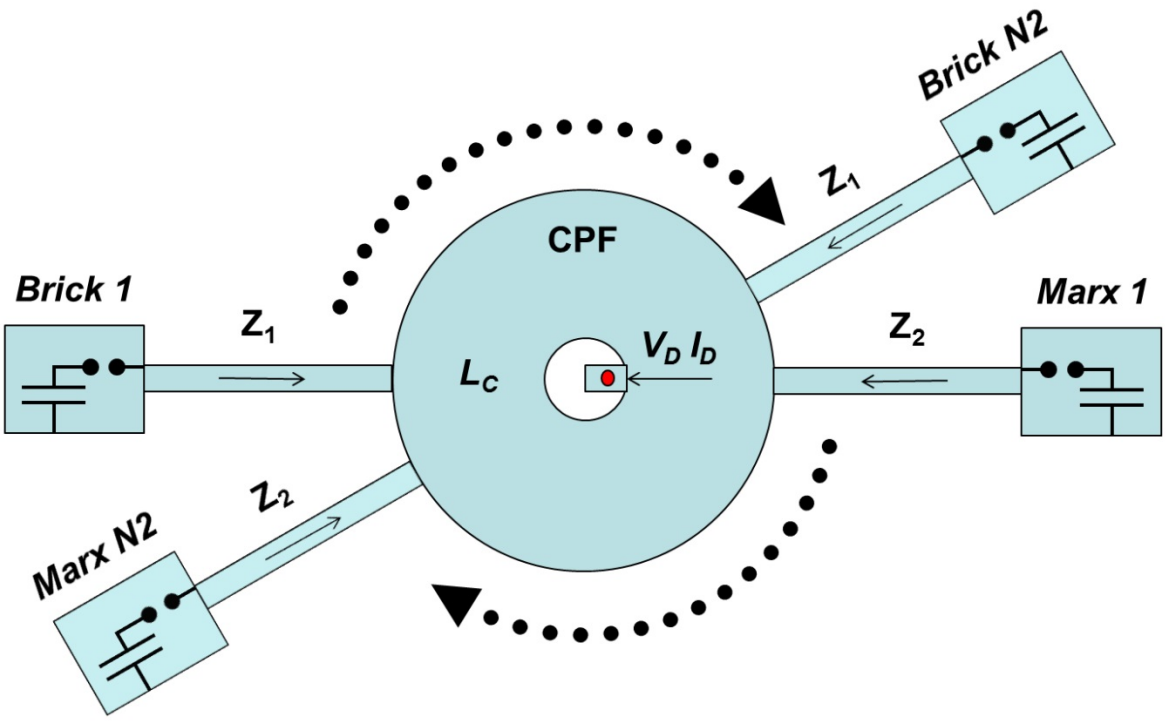

Figure 11. Conceptual representation of Thor for the mixed-brick case. Bricks 1 to N_1 represent single-stage bricks. Marx 1 to N_2 represent two-staged Marxed bricks. The equations corresponding to this " circuit-like" diagram are in Section IIIB (case b).

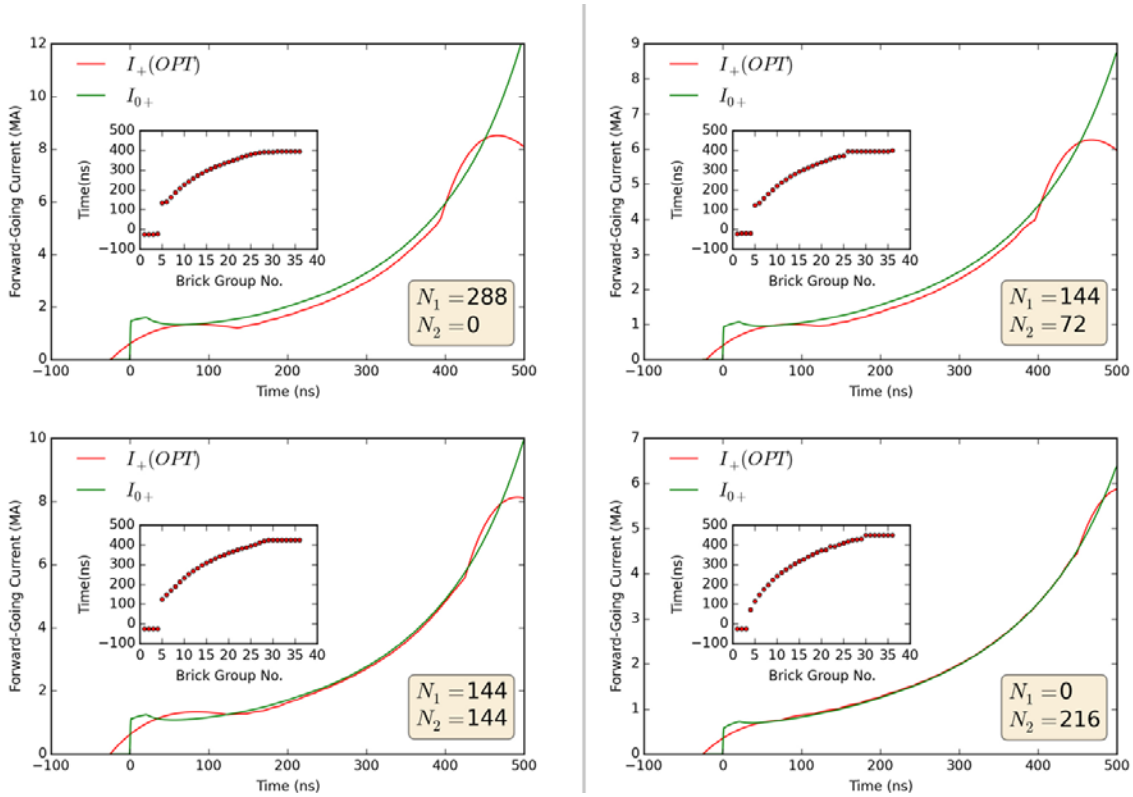

Figure 12. Aluminum optimization results with various mixed-brick options; N_1 bricks of impedance $Z_1 = 3\Omega$, and N_2 of impedance $Z_2 = 6\Omega$.

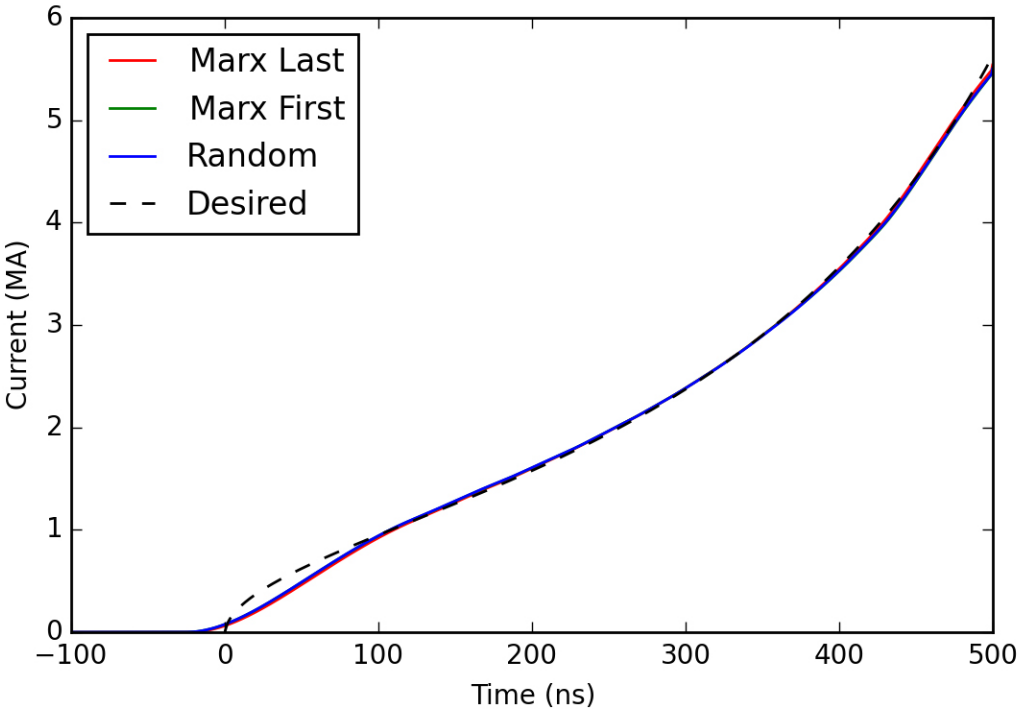

Figure 13. Desired current compared to Screamer circuit calculations with optimized trigger times for the mixed brick aluminum example $(N_1 = 144, N_2 = 144)$. Screamer calculations for the three brick-ordering combinations described in section IV.

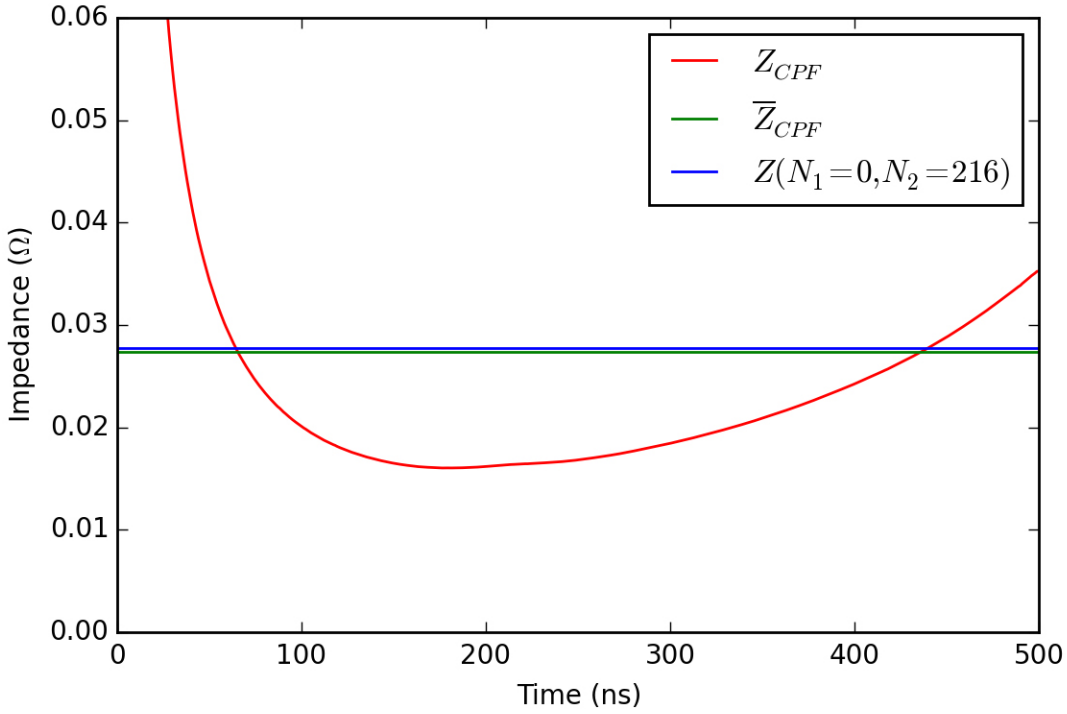

Figure 14. CPF impedance Z_{CPF}, energy-weighted CPF impedance $\overline{Z}_{CPF}$, and total cable impedance Z for the best-fit aluminum example.

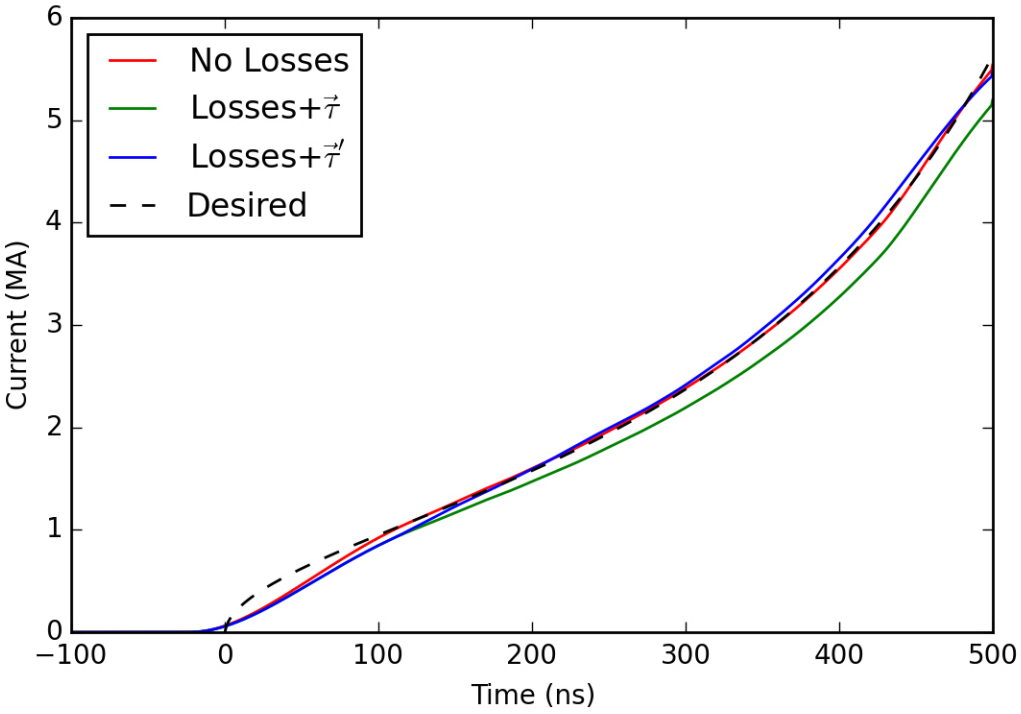

Figure 15. Desired aluminum example current waveform compared to the optimized current waveform for the following cases: (1) no cable losses; (2) cable losses and no correction in the trigger times $\vec{\tau}$; and (3) cable losses and a set of trigger times based on corrected, or attenuated, brick basis functions $\vec{\tau}'$.

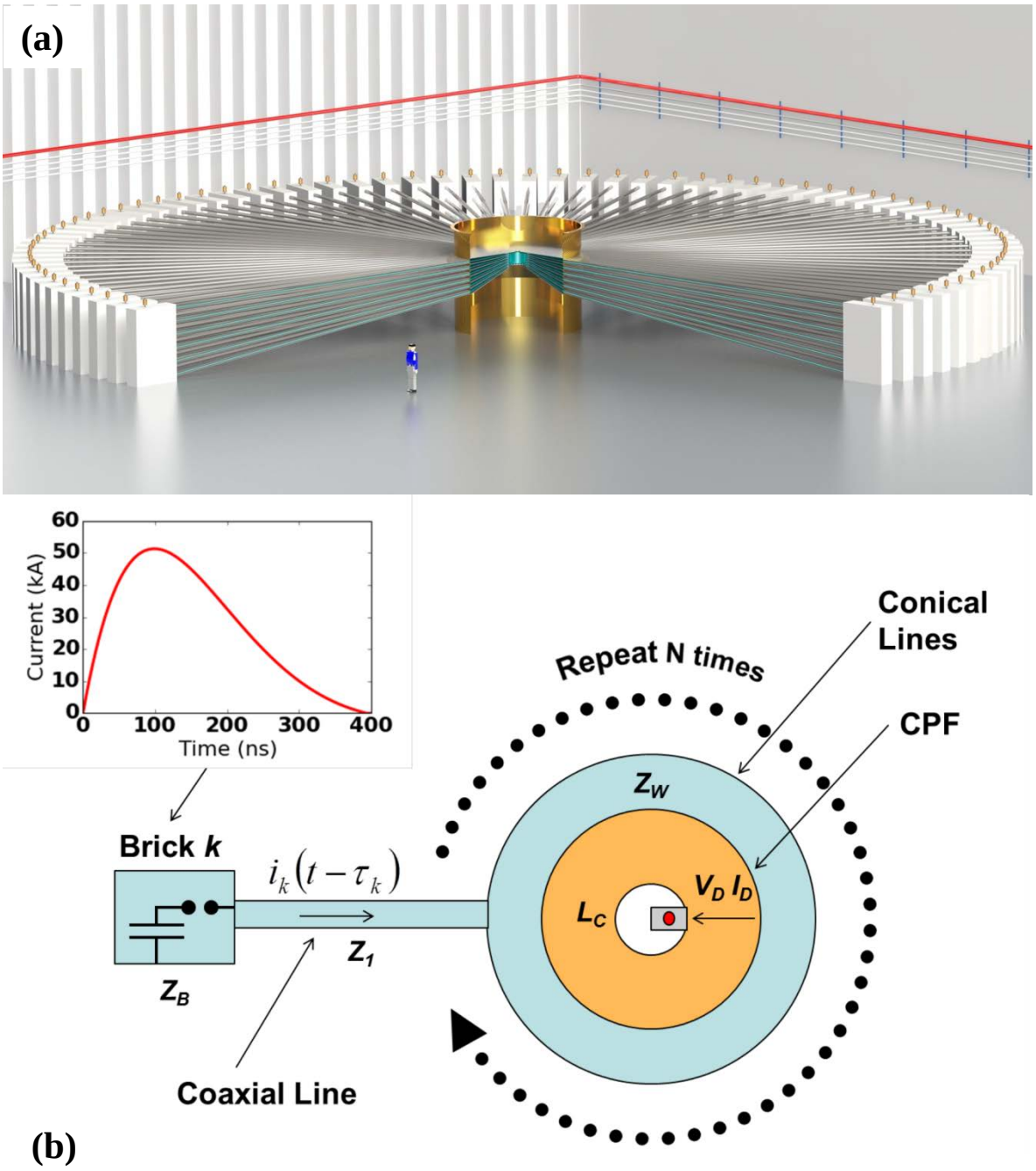

Figure 16. (a) Neptune facility design. (b) Neptune conceptual design. Single brick current waveform i(t) is also shown. N=600 bricks are connected in parallel in the Neptune design.

(a)

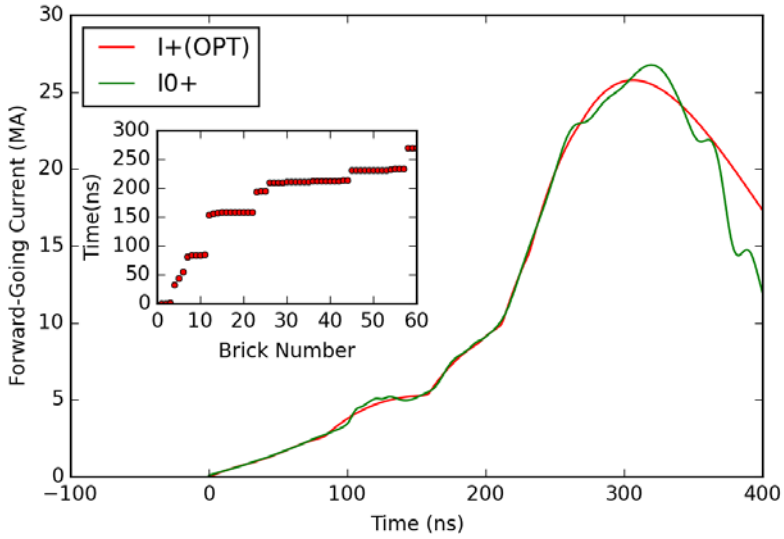

(b)

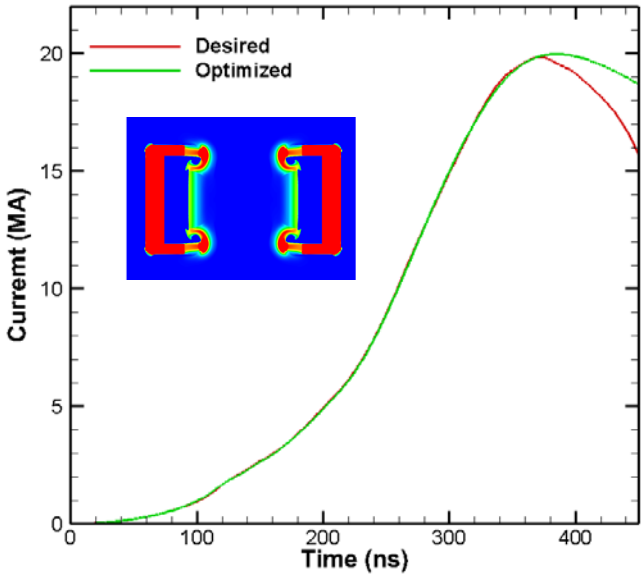

Figure 17. (a) Results of optimization using 60 brick-groups each consisting of 10 bricks. (b) Comparison of desired current to optimized current obtained by using forward-going current in the MHD code. Inset shows calculation at peak current.

(a)

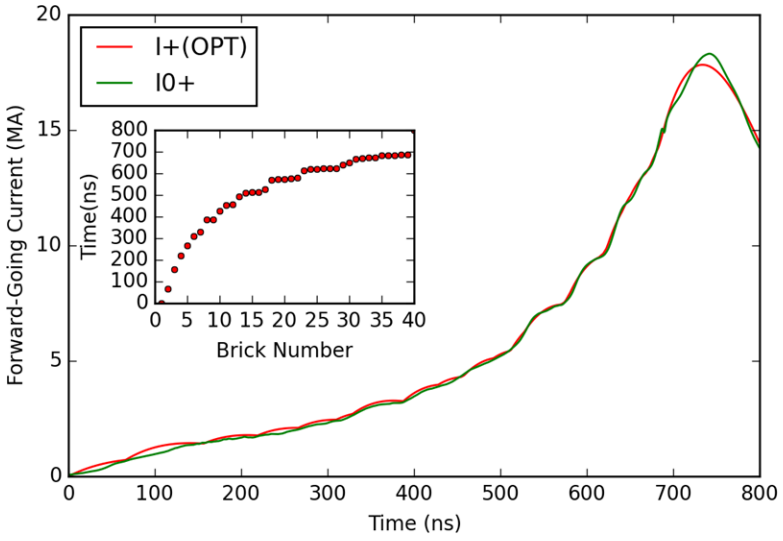

(b)

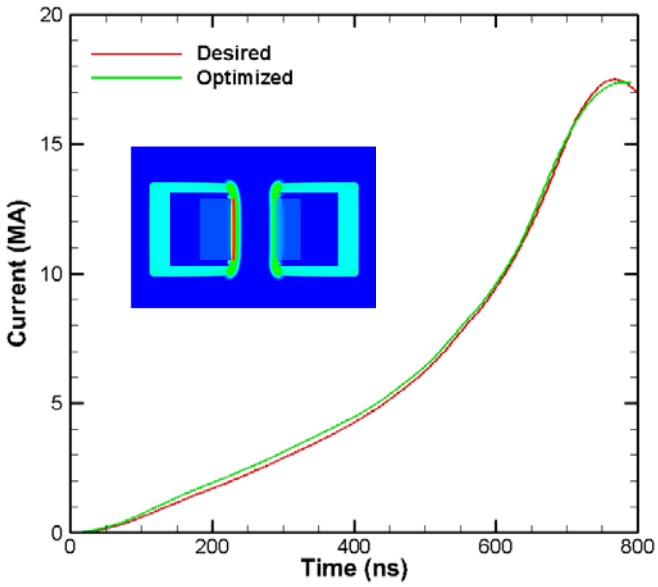

Figure 18. (a) Results of optimization using 40 brick-groups each consisting of 15 bricks. (c) Comparison of desired current to optimized current obtained by using forward-going current in the MHD code. Inset shows calculation at peak current.

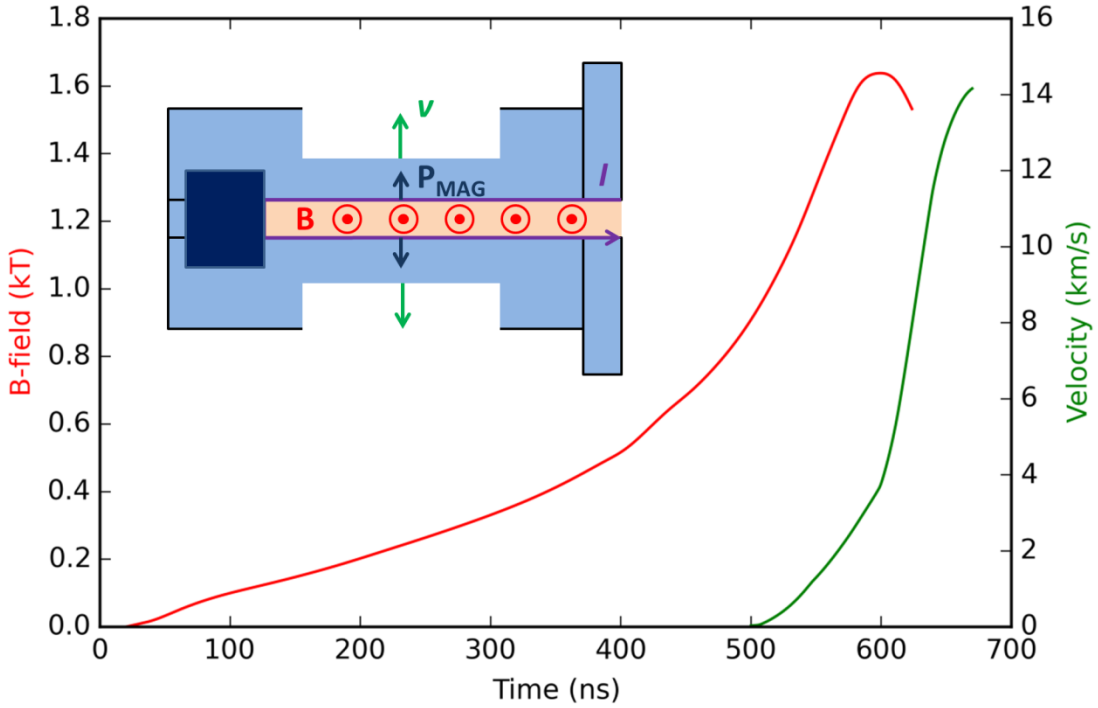

Figure 19. Optimized magnetic field waveform and resulting free-surface velocity profile of a 1.8 mm copper sample. Inset shows ICE panel arrangement.

(a)

(b)

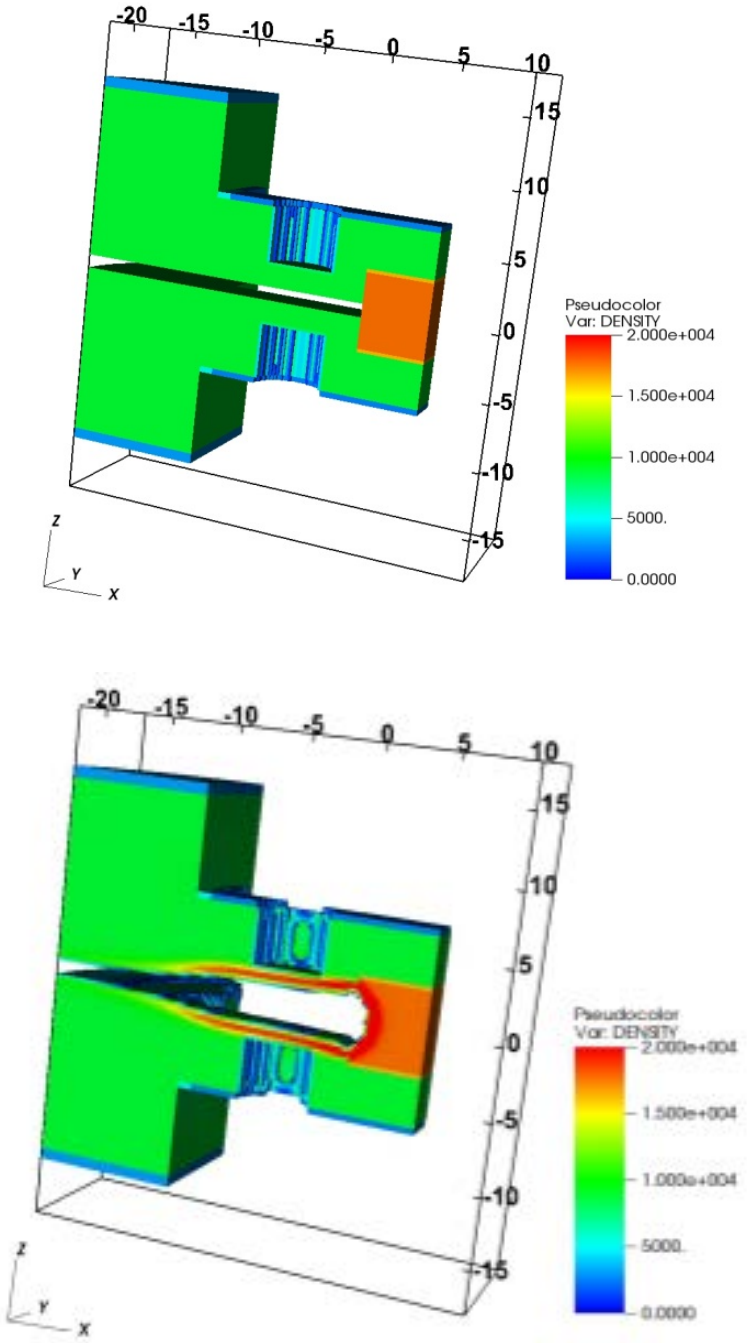

Figure 20. 3D density cross-sections of the strip-line at (a) initial time T=0 and (b) peak pressure time T=600 ns. Density is given in kg/m^3 and axes dimensions are in millimeters.

(a)

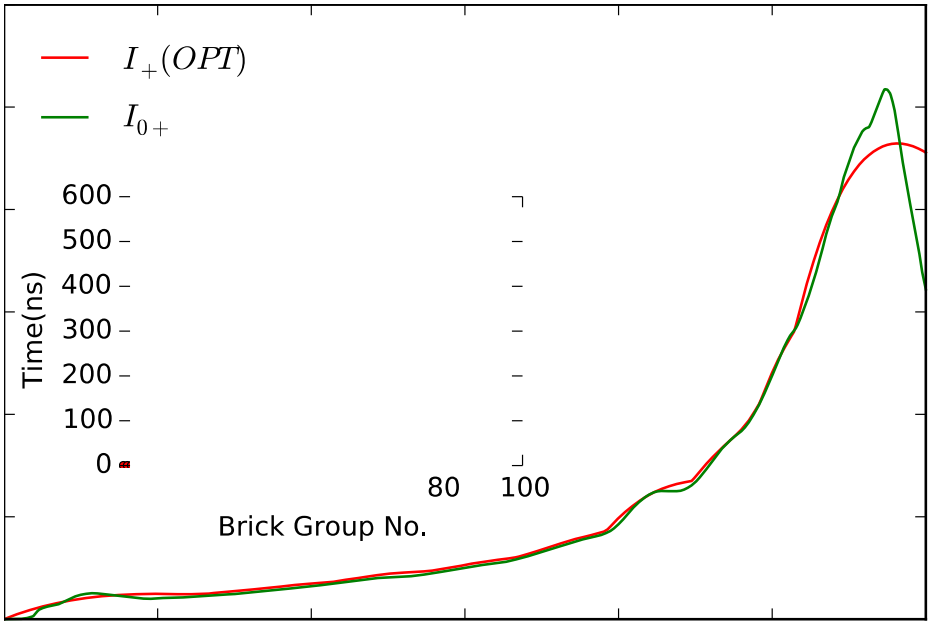

(b)

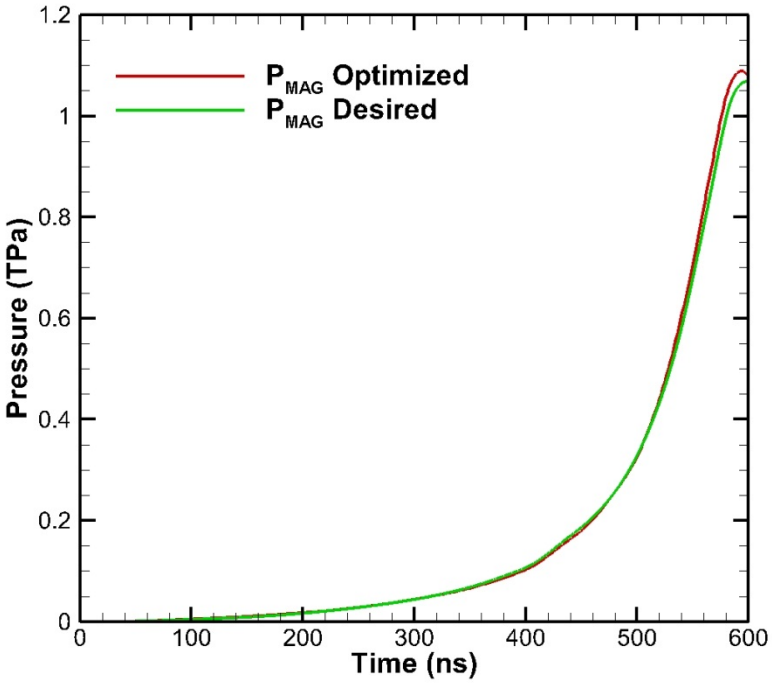

Figure 21. (a) Results of optimization using 100 brick-groups each consisting of 6 bricks. (b) Desired magnetic pressure waveform compared to pressure obtained using the optimized forward-going current in a self-consistent 3D simulation.

Table 1. Examples considered for Thor optimization

Experiment	Panel WxL (mm x mm)	Driver Thickness (mm)	Peak V (kV)	Peak I (MA)	Peak P_{MAG} (GPa)	Peak E_{LOAD} (KJ)
Copper	10 x 20	-	83.5	5.1	100	46.3
Aluminum/Cerium	15 x 30	1.0	70.4	4.27	33	29.6
Copper/Tantalum	10 x 20	1.0	70.0	5.29	89	46.3
Aluminum	10 x 20	-	147	5.61	100	62.3

Table 2. Examples considered for Neptune optimization

Experiment	Panel WxL (mm x mm)	Driver Thickness (mm)	Peak V (kV)	Peak I (MA)	Peak P_{MAG} (GPa)	Peak E_{LOAD} (MJ)
Aluminum Flyer	15 x 20	1.0	864	20.4	43.7	1.58
Copper/Tantalum	10 x 20	1.2	437	17.5	55.2	1.06
Copper	6 x 12	1.8	432	13.6	1070	1.00

DISTRIBUTION

1. MS0359 D. Chavez, LDRD Office 1911
2. MS0899 Technical Library 9536 (electronic copy)


Sandia National Laboratories